FlyOrb : Spherical Terrestrial-Aerial Bimodal Vehicle

Abstract— **Unmanned aerial vehicles perform well in aerial tasks but still face limitations due to limited endurance. In this work, we present a novel spherical terrestrial–aerial bimodal vehicle, called FlyOrb, which is capable of both rolling and flying. The vehicle integrates inertial wheel actuation with a concise mechanism based on an unactuated hinge structure, enabling quadrotor-like flight and spherical robot–like rolling. Furthermore, the mass eccentricity design allows the vehicle to be self-stabilizing on the ground but makes it difficult to initiate rolling. We propose a resonance-driven rolling strategy for activating and efficient rolling. For both slope and step, the vehicle's traversal capabilities were analyzed theoretically and tested experimentally. Thrust experiments identify the more aerodynamically efficient structure, which retains 87.2% of the thrust compared to the configuration without arm. Futher, we analyze the impact of FlyOrb's design on its flight maneuverability. Finally, flight and rolling tests validate the vehicle's multimodal locomotion capabilities. In ground mode, the average speed is 0.3505 m/s, and the power saving efficiency reaches 96.8% .**

I. INTRODUCTION

Drones, or unmanned aerial vehicles (UAVs), are widely used in military and civilian domains. Applications include logistics, surveillance, border patrol, mapping, and search and rescue [1]. However, traditional multirotor systems only have a single operation mode, which restricts their locomotion capability and endurance. To address this, terrestrial-aerial bimodal vehicles attract growing research interest. They offer enhanced flexibility and longer endurance.

Zhang et al. [2] developed a hybrid system combining rotors and four wheels for aerial-ground mobility. Similarly, Thorel et al. [3] used spherical joints for ground contact, and Pan et al. [4] proposed Skywalker, a rotor-driven single-wheel system. These designs employ passive wheels actuated by the flight module. In contrast, Tan et al. [5] and Araki et al. [6] adopted actively driven wheels. Kalantari et al. [7] introduced HyTAQ, a hybrid quadrotor using eccentric rolling. Wang et al. [8] and Zheng et al. [9] developed rotor-assisted unicycle systems. Zhang et al. [10] and Dong et al. [11] created quadrotors capable of controlled rolling with cylindrical frames. Tanaka [12], Shi [13], and Zheng [14] proposed dual-wheel rotorcraft for amphibious operation. Due to the nonholonomic constraints of wheeled structures during ground motion, they cannot generate lateral movement, making it difficult to move in confined and complex spaces. Meanwhile, Li [15], Ouyang [16], and Qin [17] integrated crawling or quadrupedal gaits with rotor flight, enhancing terrain adaptability but increasing system complexity and reducing speed. Sihite et al. [18] integrated wheeled locomotion and crawling motion to enhance terrain adaptability.In contrast, spherical robots offer omnidirectional mobility [19]. Therefore, designing aerial-ground robots based on spherical structures is a promising approach.

Several actuation strategies have been developed for spherical robots. A common method is the pendulum drive, shifting the center of mass via internal rotation [20]. Javadi et al. [21] used a mass moving along prismatic joints to achieve rotation, but this approach is hard to control. As in Bhattacharya's work [22], where internal motor torque induces shell rotation. K. Wait's design uses deformable inflatable panels to produce motion [23]. In existing designs, the actuation mechanisms occupy most of the robot's internal space and mass, making it difficult to integrate flight modules for aerial-ground operation. A compact and lightweight actuation method is therefore required.

This letter presents FlyOrb, a spherical terrestrial–aerial bimodal vehicle. The rolling drive's mass reduces flight efficiency, and its volume also limits internal component layout. To address this, we adopted a lightweight and compact inertia wheel drive. Moreover, FlyOrb requires an intentional eccentricity for stable takeoff. However, this eccentricity makes it difficult to drive the sphere. To address both the wheel's small inertia and the sphere's eccentricity, we proposed a resonance-driven rolling strategy [24], [25]. We adopted simple unactuated hinges to realize the transformation between spherical and quadrotor modes. The arms deploy passively when the propeller activates, slightly reducing flight agility [26]. Resonance-driven rolling and unactuated hinges are the key technologies enabling FlyOrb.

This letter is organized as follows. Section II details the vehicle design. Section III establishes dynamics equations for the inertia wheel drive. It verifies resonance-driven motion feasibility through numerical simulations and physical experiments. Motion strategy selection for flight and ground rolling is analyzed in two representative environments. Section IV first conducts rotor thrust tests, and a more aerodynamically efficient arm design is selected. Furthermore, the impact of FlyOrb's design on its flight maneuverability is also analyzed. Experiments validate both flight and rolling capabilities of the proposed vehicle. Finally, we compare FlyOrb with other works of different configurations.

II. VEHICLE DESIGN

FlyOrb primarily aims to integrate a quadrotor UAV with a spherical rolling robot. This combines the ground mobility of a spherical robot with the maneuverability of a quadrotor.

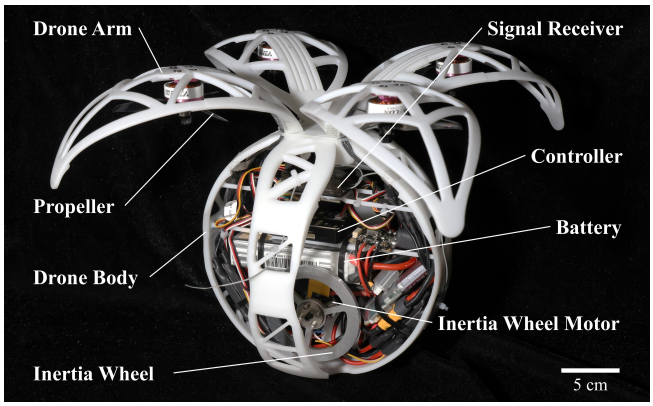

Fig. 1. FlyOrb hardware configuration

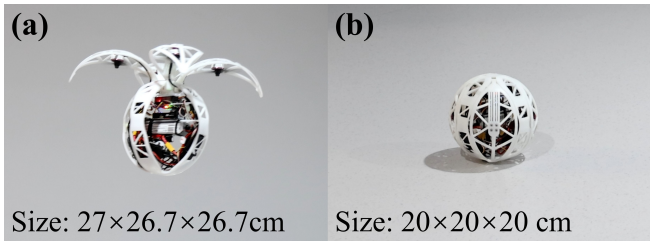

Fig. 2. Two forms of FlyOrb: (a) Flying mode (b) Rolling mode

A. Mechanical Design

FlyOrb is a spherical terrestrial–aerial bimodal vehicle. It achieves cross-medium motion through ground rolling and aerial flight modes. Fig. 1 shows its hardware configuration. When folded (Fig. 2(b)), the body and four arms form a sphere. The body connects to the arms via unactuated hinges. Magnets hold the arms closed. The motor attached to the body drives the inertia wheel's rotation. This generates reactive torque on the body, enabling ground rolling through resonance-driven motion. During ground operation, internal component placement creates an eccentric mass distribution. This design like a roly-poly toy offers automatic balance recovery. It also ensures attitude stability during takeoff, enabling successful arm deployment.

As shown in Fig. 2(a), the motors drive the four rotors. This generates sufficient aerodynamic lift. The lift produces aerodynamic torque, causing the arms to extend. In consideration of the limited space between the body and the arms, the plane of the rotors is perpendicular to the body's axis. In this state, the aircraft resembles a conventional quadrotor drone.

B. Resonance-driven Rolling Design

The body's center of mass differs from the sphere's geometric center. This makes the system an eccentric sphere with self-stabilizing characteristics. An actuation torque acts on the body, then gravity creates a restoring torque. This causes the body to oscillate nonlinearly around its original position. Resonance-driven motion is highly efficient, as the applied force direction aligns with the velocity direction.

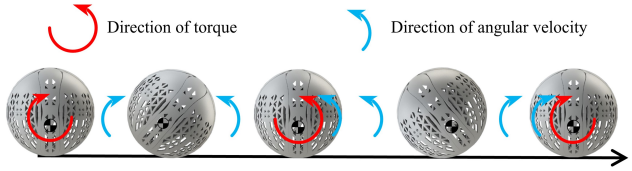

Fig. 3. Schematic of the resonance-driven strategy.

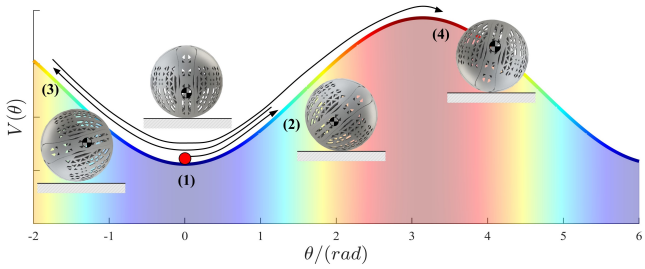

Fig. 4. Potential energy variation during the initiation of rolling.

This alignment keeps power positive, which ensures energy continuously flows into the system.

This concept extends to the sphere's nonlinear oscillations. As shown in Fig.3, the resonance-driven strategy for the inertia wheel is simple and effective: Each time the body passes through its equilibrium position, its angular velocity is maximum. At this instant, the inertia wheel immediately reverses and accelerates. This applies a short-duration impulse torque to the body. This impulse torque aligns with the body's angular velocity direction. Over several oscillation cycles, the torque continuously does positive work on the body. When the kinetic energy becomes sufficient, the body's rotation angle exceeds 180°. The sphere then overcomes this potential energy peak. Finally, it begins to roll forward. Fig.4 shows the potential energy during rolling initiation.

C. Electronic System

Fig. 5 shows FlyOrb's electronic system. A single 4S lithium polymer battery powers the system. This connects to a distribution board, which provides multiple parallel power outputs for flight controller and electronic speed controllers (ESCs). The ESCs adjust motor speeds based on signals from the flight controller. The flight controller is a CUAV V5 NANO. The flight module uses AE2207 brushless motors (5 mm shaft, 31.4 g). These pair with Gemfan 4032 three-blade propellers (102.2 mm diameter). This combination meets the arms' limited internal space requirements. Each motor uses a 40A ESC for precise control. The rolling module employs an A2212 brushless motor (56 g, 22 mm stator diameter). It couples with an aluminum alloy inertia wheel (80 g, 80mm diameter). The remote control system includes a Ledar AT10 transmitter and R12DS receiver, which provides reliable signal transmission.

D. Manufacturing

The vehicle's main structure includes the body and arms. It is fabricated using white photosensitive resin. This uses stere-

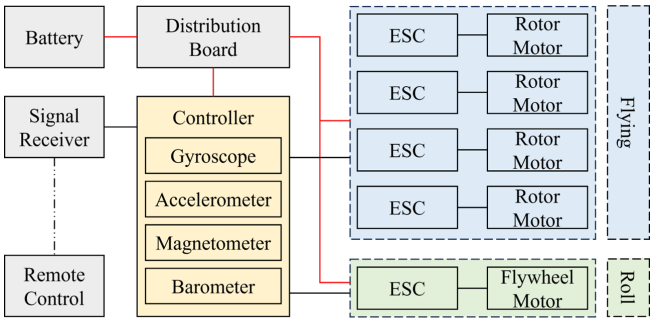

Fig. 5. Overview of electronics for FlyOrb

olithography (SLA) 3D printing. This photopolymerization-based technique provides tolerance of ±0.1 mm. It also ensures good structural consistency. Other components are universal products. These include connectors, motors, batteries, flight controllers and the inertia wheel.

III. DYNAMICS MODELING AND ANALYSIS

In this section, we develop the driven sphere's dynamic equations using the Lagrangian method. Both simulations and experiments verify the feasibility of resonance-driven motion for rolling. We also analyze motion scenarios: rolling uphill and overcoming steps. This analysis enables the system to decide when to switch to flight mode based on environmental parameters.

A. Resonance-driven Rolling

In the closed-arm state, FlyOrb operates as an eccentric sphere. Dynamic modeling is firstly established to simulate the effective driving. Here, the sphere's center of mass is considered stays within the same vertical plane D and both the inertia wheel and sphere rotate in planar motion. Thus, this problem simplifies to a two-dimensional planar system. We assume sufficient ground friction coefficient. This prevents relative slipping between sphere and ground. Therefore, the sphere's motion simplifies to one degree of freedom.

The dynamic equation of the inertia wheel-driven sphere is derived using Lagrange's equation, as shown in Fig. 6(1). Here, O represents the center of the sphere; C denotes the center of mass of the sphere; m is the mass of the body; m_1 is the mass of the inertia wheel; R is the radius of the sphere; r is the eccentric distance; l is the distance from the center of the inertia wheel to the center of the sphere; τ is the torque applied by the motor to the body; and M_f is the rolling resistance torque acting on the sphere from the ground. J_o is the moment of inertia of the body rotating about its horizontal diameter, while J_w is the moment of inertia of the inertia wheel about its rotation axis.

This planar system considers only two-dimensional motion. We assume pure rolling contact between sphere and ground. Thus, the two-body system has two degrees of freedom. The generalized coordinates are θ and ϕ. Here, θ is the body's angle relative to the ground coordinate and ϕ is the inertial wheel's angle relative to the ground coordinate. The

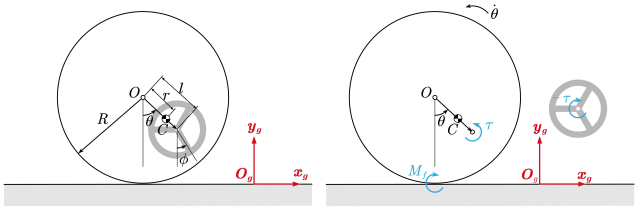

Fig. 6. Rolling dynamics model picture

system's kinetic energy combines the body's kinetic energy and the inertial wheel's kinetic energy.

$$T = T_W + T_O = \frac{1}{2}\begin{bmatrix}\dot{\theta} & \dot{\phi}\end{bmatrix}\begin{bmatrix}A & 0\\ 0 & B\end{bmatrix}\begin{bmatrix}\dot{\theta}\\ \dot{\phi}\end{bmatrix} \tag{1}$$

Where

$$\begin{cases} A = m_1\left(R^2 + l^2 - 2Rl\cos\theta\right) \\ \quad\quad + m\left(R^2 - 2Rr\cos\theta\right) + J_o \\ B = J_W \end{cases} \tag{2}$$

The potential energy of the system is expressed as

$$V = mg\left(R - r\cos\theta\right) + m_1 g\left(R - l\cos\theta\right) \tag{3}$$

Fig. 6(2) shows the system affected by non-conservative forces. The inertial wheel is subjected to the torque from the motor. The body is affected by two torques: the reaction torque τ from the motor and the rolling resistance couple M_f from the ground.

By substituting the Lagrangian function $L = T - V$ into the Lagrange equation

$$\frac{\mathrm{d}}{\mathrm{d}t}\left(\frac{\partial L}{\partial \dot{q}_j}\right) - \frac{\partial L}{\partial q_j} = Q_j', j = 1, \cdots, k \tag{4}$$

After calculation, the dynamic equations are obtained as follows:

$$\begin{cases} C\ddot{\theta} + D\sin\theta + E\dot{\theta}^2\sin\theta = M_f + \tau \\ J_W\ddot{\phi} = -\tau \end{cases} \tag{5}$$

Where

$$\begin{cases} C = m_1\left(R^2 - 2Rl\cos\theta + l^2\right) + m\left(R^2 - 2Rr\cos\theta\right) \\ \quad\quad + J_o \\ D = gmr + gm_1 l \\ E = Rm_1 l + Rmr \\ M_f = \delta\left(mr + m_1 l\right)\left(\ddot{\theta}\sin\theta + \dot{\theta}^2\cos\theta\right) \\ \quad\quad + \delta\left(m_1 + m\right)g \end{cases} \tag{6}$$

The complete dynamic equations for the two-body system are established. Based on the dynamic equations, the motion process can be computed using the 4th-5th order Runge-Kutta (RK45) numerical method, with the parameter values listed in TABLE I.

Fig.7(a) shows the body's rotation angle θ with respect to time t. The experimental procedure is shown in Fig.17. The black dashed line represents the boundaries θ=180° . When the rotation angle θ reaches the boundary and the angular velocity is non-zero, it indicates that the body can overcome

TABLE I

ROLLING MODE PARAMETERS AND THEIR VALUES

Parameters	Value	Unit
m	1.09	kg
R	0.1	m
r	0.005	m
J_o	0.024	kg·m^2
l	0.04	m
m_1	0.08	kg
J_w	5e-4	kg·m^2
δ	1e-4	m

the potential energy barrier and roll in a specific direction. At t=10.9 s, θ=180°. During oscillations, the inertia wheel applies multiple short-duration pulse torques to the body by switching its direction. The pulse torque aligns with the body's angular velocity, leading to a gradual increase in the body's rotational amplitude until it reaches the critical position.

Fig.7(b) illustrates numerical simulation results of the body's kinetic energy, potential energy, and total energy. It can be observed that during the body's oscillatory motion, the kinetic and potential energies fluctuate inversely. Our strategy applies short-duration pulse torques when the inertia wheel reverses direction at the body's equilibrium position. As a result, the kinetic energy briefly increases when the potential energy V reaches its minimum at the equilibrium position. Without external torque, total energy gradually decreases. This also shows energy dissipation from rolling friction between body and ground.

Furthermore, the effect of eccentricity on the sphere's dynamic characteristics is analyzed through solving the dynamic equations. A larger eccentricity makes the sphere harder to drive under the same configuration, but it improves self-stability. Therefore, eccentricity is a key dynamic parameter of FlyOrb. We analyzed different nondimensional eccentricities r/R to generalize the results. As shown in Fig.8, a larger center of mass eccentricity requires more drive actions to start rolling. This leads to longer startup time and higher energy use. At the same time, the maximum self-righting time becomes shorter, indicating better stability.

B. Uphill Strategy Selection

If the FlyOrb encounters an uphill slope, it must either roll up the slope using resonance-driven rolling or switch to the flight mode to fly over it. Such decision depends on the parameters of the specific motion scenario. As shown in Fig.9, the distance the sphere rolls before contacting the slope surface is d, the slope angle is α, and the slope length is L. Three assumptions are made for the analysis:

1) Only the motion of the sphere rushing up the slope due to its inertia is considered, and the torque exerted by the inertia wheel on the sphere is neglected.
2) The coefficient of friction between the sphere and the ground is sufficiently large to prevent slipping.
3) The collision between the sphere and the slope is neglected, and it is assumed that there is no loss of kinetic energy as the sphere transitions from the horizontal surface to the slope.

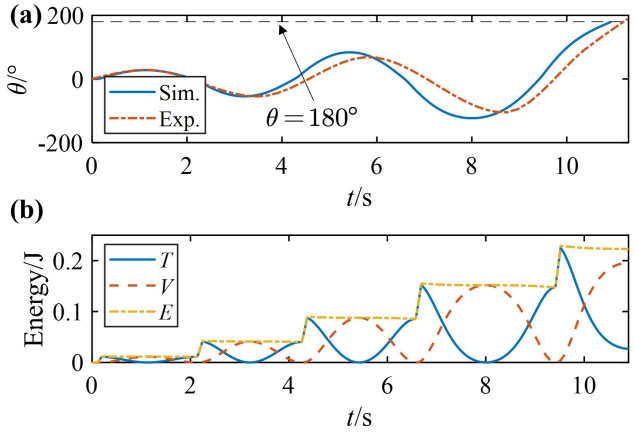

Fig. 7. Numerical simulation and experimental results of the rolling process: (a) θ vs. time ; (b) Energy vs. time

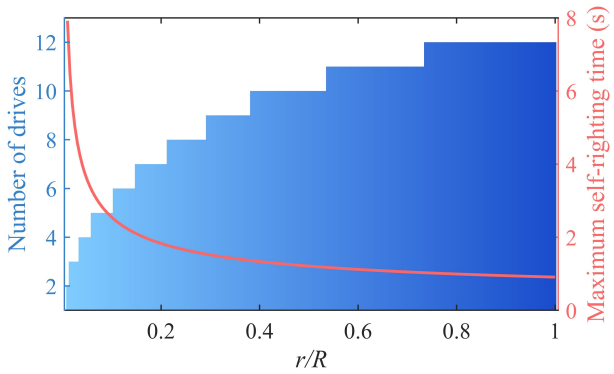

Fig. 8. Number of drive actions to start rolling and maximum self-righting time versus eccentricity r/R

To analyze the motion process, we calculate the angular velocity of the sphere after it advances a distance d starting from rest. This angular velocity corresponds to the kinetic energy E_k at the base of the slope. As the sphere rolls up toward to the slope, the kinetic energy is converted into gravitational potential energy. The change in potential energy is contributed to two factors: the height change along the slope and the eccentricity of the sphere's center of mass during rotation.

The gravitational potential energy at the base of the slope is given by:

$$E_{p0} = mg\left(R - r\cos\left(d/R\right)\right) \tag{7}$$

After rolling a distance x along the slope, the gravitational potential energy becomes:

$$E_p(x) = mg\left(x\sin\alpha + R\right) - mgr\cdot\cos\left(\frac{d+x}{R}\right), x \in [0, L] \tag{8}$$

Therefore, the condition $E_k \geqslant \max\left(E_p\left(x\right)\right) - E_{p0}$ must hold for the sphere to roll up the slope. Otherwise, it cannot ascend and must switch to flight mode. This criterion determines the feasible rolling region under different environmental parameters. As shown in the Fig.10, each angle

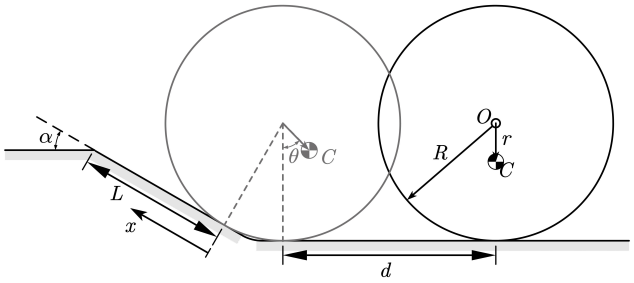

Fig. 9. Parameters during the FlyOrb rolling-up-the-slope process.

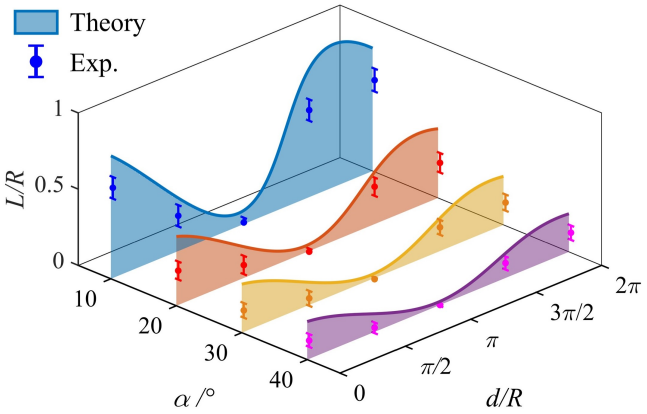

Fig. 10. Maximum climbing distance on slopes under different startup distances and slope angles, including both theoretical and experimental results.

corresponds to a curve. The colored area shows the feasible rolling region for slope ascent. We also conducted experiments. As the figure shows, the actual climbing distance was shorter than the theoretical prediction due to the idealized assumptions. However, the experimental data and theoretical analysis show similar trends. This agreement validates our theoretical model qualitatively.

The sphere reaches maximum speed when its center of mass is at the lowest point ($d = 0$ and $2\pi R$); elsewhere, it must overcome gravitational potential energy, an effect most pronounced at $d = \pi R$ where the potential energy at the bottom is highest. As d increases, the kinetic energy at the bottom first decreases and then increases. For zero eccentricity ($r = 0$), the travel distance L under a fixed slope angle would be positively correlated with this kinetic energy and thus expected to first decrease and then increase with d. However, Fig. 10 shows a deviation due to eccentricity: L first decreases, then increases, and finally decreases again. This results from the varying center-of-mass position when the sphere reaches the bottom, which alters the gravitational potential energy profile during rolling.

C. Step-Climbing Strategy Selection

Similarly, FlyOrb may encounter a step barrier, and Whether if it can roll over the step also depends on the motion scenario's parameters. See Fig. 11. Here, d is the

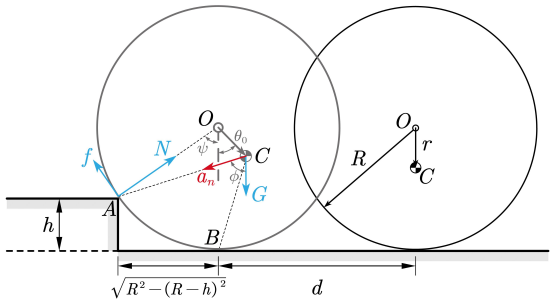

Fig. 11. Parameters during the FlyOrb step-climbing process.

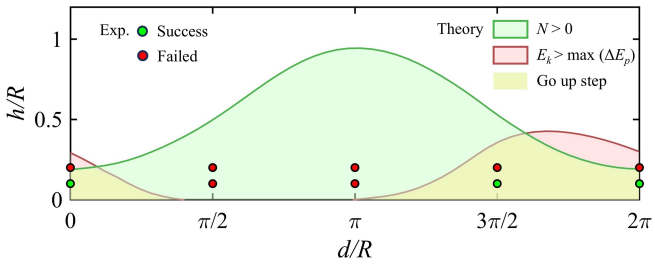

Fig. 12. Feasibility analysis of step-crossing under different startup distances and step heights, including both theoretical and experimental results.

distance the sphere travels. h is the step height. G is the sphere's weight. N is the support force at contact point A. The normal direction of the contact corresponds to the direction of the support force N. The angle ψ denotes the angle between AO and the vertical direction, while ϕ denotes the angle between AC and the vertical direction. Three assumptions are used in the analysis:

1) Only the motion of the sphere rushing up the step due to its inertia is considered, and the torque exerted by the inertia wheel on the sphere is neglected.
2) The coefficient of friction between the sphere and both the ground and the edge of the step is sufficiently large to prevent any relative sliding between the sphere and the surfaces.
3) The sphere undergoes a perfectly inelastic collision at the edge of the step.

During the collision between the sphere and the step, the angular momentum of the sphere about the axis passing through point A is conserved. Therefore, the following equation holds

$$\vec{r}_{AC} \times m(\omega_0 \times \vec{r}_{BC}) + J_C \omega_0 = J_A \omega \tag{9}$$

$$\vec{r}_{AC} = \begin{bmatrix} \sqrt{R^2-(R-h)^2} + r\sin\theta_0 \\ R - h - r\cos\theta_0 \end{bmatrix}$$
$$\vec{r}_{BC} = \begin{bmatrix} r\sin\theta_0 \\ R - r\cos\theta_0 \end{bmatrix} \tag{10}$$

The first term on the left side of the equation shows the angular momentum of the sphere's center of mass relative to point A. The second term shows the angular momentum relative to the center of mass. On the right side is the angular momentum of the sphere relative to point A. ω_0 and ω

stand for the angular velocities before and after the collision, respectively. The sphere's kinetic energy can be written as $E_k = \frac{1}{2} J_A \omega^2$. During the collision, the sphere's gravitational potential energy is:

$$E_{p0} = mg\left(R - r\cos\left(\theta_0\right)\right), \theta_0 = d/R \tag{11}$$

When the sphere rotates by an angle $\Delta\theta$ around the point A, the gravitational potential energy of the sphere is:

$$\begin{aligned} E_p\left(\Delta\theta\right) = mg\Big[&h + \sqrt{R^2 - \left(R-h\right)^2}\sin\Delta\theta \\ &+ \left(R-h\right)\cos\Delta\theta - r\cos\left(\Delta\theta + \theta_0\right)\Big] \end{aligned} \tag{12}$$

$$\Delta\theta \in [0, \phi], \phi = \arctan\left(\frac{\sqrt{R^2 - \left(R-h\right)^2} + r\sin\theta_0}{R - h - r\cos\theta_0}\right) \tag{13}$$

So, the condition for the sphere to be able to roll over the step is:

$$E_k \geqslant \max\left(E_p\left(\Delta\theta\right)\right) - E_{p0} \tag{14}$$

In the above derivation, we aim for maximum kinetic energy in the sphere from an energy perspective. But when the sphere's angular velocity is very high, the centripetal force needed for rotation around point A increases. If the gravitational force component cannot provide sufficient centripetal force, the sphere will detach from point A. It will then fail to roll over the step.

During rotation around point A, the angular velocity decreases. This reduces the required centripetal force. At the same time, the gravitational force component along AC increases. Thus, if the condition $N > 0$ is satisfied immediately after the collision, the sphere will not detach from point A throughout the entire process.

The equation of motion for the center of mass in the N direction is:

$$\begin{aligned} G\cos\psi - N &= m\omega^2 \overline{AC}\cos\left(\phi - \psi\right), \\ \psi &= \arccos\left(\frac{R-h}{R}\right) \end{aligned} \tag{15}$$

The condition for the sphere to remain attached at point A is:

$$N = G\cos\psi - m\omega^2\overline{AC}\cos\left(\phi - \psi\right) > 0 \tag{16}$$

Therefore, FlyOrb can only roll over the step if both conditions in Equation(14) and Equation(16) are satisfied. Based on this, we define the feasible rolling region under different environmental parameters. As shown in Figure 12, the parameter range below the green curve represents conditions for the sphere to remain attached at point A. The range below the red curve represents conditions where kinetic energy is sufficient to overcome gravitational potential energy. Only within the yellow region does the speed fall in an optimal range, enabling the sphere to roll over the step successfully.

Further, we tested the sphere's ability to climb steps of heights $0.1R$ and $0.2R$ with varying starting distances d. Experimental results shows that the actual obstacle-crossing capability is weaker than theoretically predicted. During experiments, we observed noticeable sliding between the sphere and step edge. Since our theoretical model assumes sufficient friction to prevent such sliding, this observed slip is a primary source of the error. For the $0.1R$ step, however, experimental results match theoretical predictions well, supporting the validity of our model. Step terrain is challenging for FlyOrb. Its inertia wheel drive cannot provide continuous torque. The robot can only climb steps by relying on inertia.

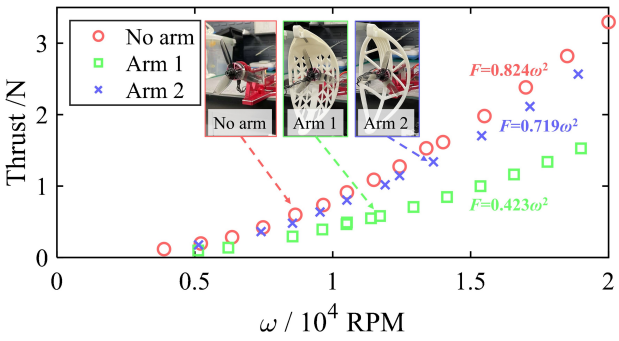

Fig. 13. Experimental results of thrust tests for rotors under different arms and without arms.

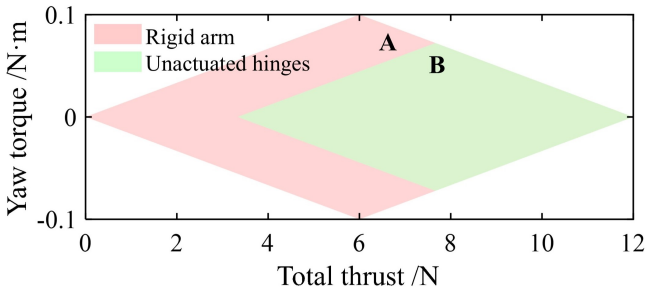

Fig. 14. In the flight state of the aircraft, the feasible range of total thrust and yaw torque when roll and pitch torques are zero. The green feasible region B with unactuated hinges is a subset of the red feasible region A for rigid arms.

IV. RESULTS AND DISCUSSION

A. Force Experiments on the Propellers

To evalate how the arm above the rotor impacts aerodynamic efficiency, we designed two arm types. The experiment used a Gemfan 4032 propeller. We measured rotor thrust at different motor speeds under three conditions. Experimental setup and results are shown in Fig.13. An arm above the rotor reduces the rotor's aerodynamic efficiency. Specifically, thrust with Arm 1 installed is 51.36% of that without an arm, while thrust with Arm 2 installed is 87.2% of that without an arm. Thus, Arm 2 has better aerodynamic efficiency.

B. Flight Maneuverability Analysis

In this work, FlyOrb uses unactuated hinges, and its center of mass lies below the rotor plane. Therefore, we analyze how these two factors affect its flight maneuverability.

We studied the feasible range of total thrust and available yaw moment under zero roll and pitch moments. Consider a single rotor thrust $f_i \in [f_{\min}, f_{\max}]$. For unactuated hinges, $f_{\min}$ equals the weight of a single arm, while for rigid arms

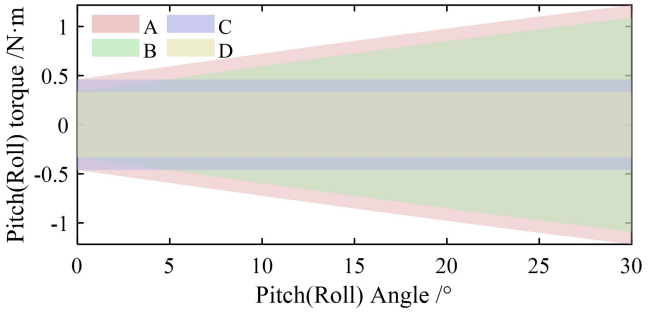

Fig. 15. Pitch (roll) moment range at different pitch (roll) angles. Four configurations: A (rigid arm, CoM(center of mass) below rotor plane), B (unactuated hinge, CoM below rotor plane), C (rigid arm, CoM at rotor plane), D (unactuated hinge, CoM at rotor plane).

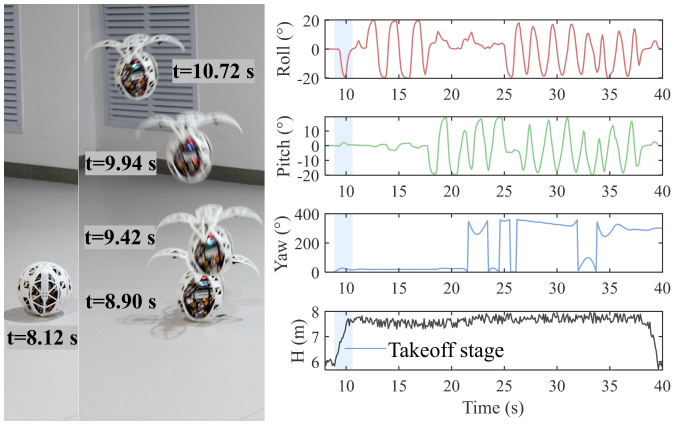

Fig. 16. FlyOrb's takeoff process and the changes in pitch angle, roll angle, yaw angle, and height over time.

$f_{\min} = 0$. Assume a single rotor has drag torque $\tau_i = kf_i$ with $f_i \in [f_{\min}, f_{\max}]$. The boundary linear equations for the feasible region of total thrust and yaw moment are $\tau_{\text{yaw}} = \pm k(T_{\text{total}} - 4f_{\min})$ and $\tau_{\text{yaw}} = \pm k(T_{\text{total}} - 4f_{\max})$. Results are shown in Fig. 14. Feasible region B (with unactuated hinges) is a subset of feasible region A (for rigid arms).

Furthermore, we analyzed the pitch and roll motions. Depending on whether unactuated hinges are used and on the position of the center of mass relative to the rotor plane, four configurations can be defined. We calculated the pitch (roll) moment range at different pitch (roll) angles. The wheelbase is a, the distance between the center of mass and the rotor plane is b, and the pitch angle is α. The upper and lower bounds of the moment range are given by $\tau_{\text{pitch}} = \pm\left[a(f_{\max} - f_{\min})/\sqrt{2} + mgb\sin\alpha\right]$. Since the pitch and roll angles remain small during motion, only the range of 0–30° is considered. All related parameters, including thrust, wheelbase, and the distance between the center of mass and rotor plane, are based on FlyOrb's specifications. As shown in Fig.15. The use of unactuated hinges reduces the maximum pitch (roll) moment, while a lower center of mass provides a stronger restoring moment.

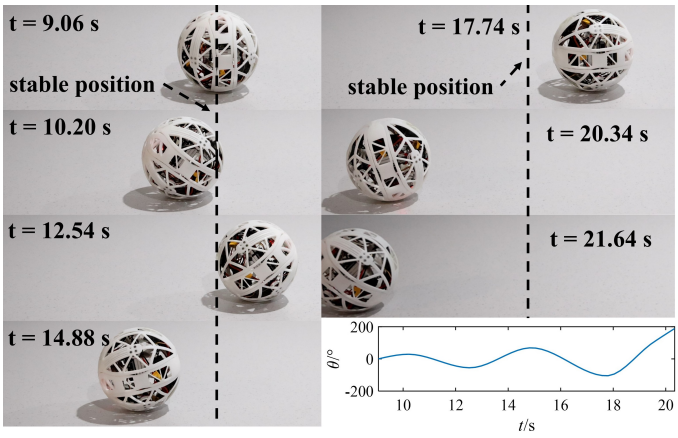

Fig. 17. FlyOrb's resonance-driven process and the variation of rotation angle over time.

C. Prototype Test

In the flying test, we tested the vehicle's arm deployment from the ground, followed by takeoff and flight. At the equilibrium position, aerodynamic forces from the rotors make the arms rotate. This initiates the opening of all four arms. By further increasing rotor speed, the vehicle takes off vertically under rotor-generated aerodynamic forces—similar to a conventional quadcopter. Results are shown in Fig.16.

In the rolling test, we tested the vehicle's forward rolling motion. It is initiated by resonance-driven rolling while the arms stay closed. First, the vehicle is stationary on the ground. After several vibration cycles, the counter torque continuously does positive work on the body. Eventually, when kinetic energy is enough to make the body's rotational angle exceed 180°, it has surpassed the highest potential energy point. The vehicle can then start rolling forward, as illustrated in Fig.17. We also measured the rolling speed multiple times, and the calculated rolling speed was 0.3505±0.0137 m/s. The 95% confidence interval calculated based on the t-distribution was [0.3124, 0.3887] m/s.

FlyOrb uses a 80 g inertial wheel to drive the full 1.17 kg system. The complete drive assembly weighs only 136 g, just 11.6% of the total mass. Through experimental measurements and calculations, the average rolling power of FlyOrb is 7.22 W, and the power during aerial hovering is 231.99 W. So the power saving efficiency is 96.8%.

D. Benchmark Comparison

In this subsection, we compare FlyOrb with other representative works of different configurations (Table II). The definitions of indicators are as follows:

1) Switching Speed: Time for the vehicle to complete aerial-ground mode transition.

2) Ground Extra Mass Ratio: Ratio of ground locomotion components mass to total vehicle mass.

3) Energy Efficiency: Energy advantage of ground over aerial mode, calculated as $1 - P_g/P_a$ (P_g: ground power, P_a: aerial power).

TABLE II

THE TABLE OF THE BENCHMARK

	Proposed	Pan et al.[4]	Tan et al.[5]	Zhang et al.[10]	Sihite et al.[18]
Switching Speed	≈2.6s	≈0s	≈5s	≈1s	≈5s
Ground Extra Mass Ratio	11.6%	12.5%	66.7%	16.6%	54.4%
Energy Efficiency	96.8%	75.2%	58.3%	85.7%	96.6%
Mode Switch	Passive	Not required	Not required	Not required	Active

4) Mode Switch: Approach for aerial-ground mode transition.

FlyOrb achieves the lowest ground extra mass ratio (11.6%) and highest energy efficiency (96.8%) among compared works. Because FlyOrb requires the deployment of the arm passively for its transformation, the switching speed is slightly lower than that of some other works.

V. CONCLUSION

This letter presents FlyOrb, a spherical terrestrial–aerial bimodal vehicle. It integrates both quadrotor flight and resonance-driven rolling. Arms are connected to the body via unactuated hinges, allowing passive folding and deployment. Sphere's dynamics are modeled using the Lagrange equation, which forms the basis of the resonance-based rolling strategy. For both slope and step, the vehicle's traversal capabilities were analyzed theoretically and tested experimentally. The aerodynamic impact of arm design is investigated through experiments to identify a configuration. A further quantitative analysis is conducted to assess the impact of FlyOrb's design on flight maneuverability. Flight experiments demonstrate stable performance, while rolling trials validate the method, achieving an average speed of 0.35 m/s on flat ground.

Future work will improve the rolling drive system for omnidirectional movement on the ground. The power and control systems will be miniaturized to reduce weight and size. Additional sensing and computing modules will be added to achieve autonomous navigation in complex environments.

REFERENCES

[1] P. Agrawal, P. Jawarkar, K. Dhakate, K. Parthani, and A. Agnihotri, "Advancements and challenges in drone technology: A comprehensive review," in *2024 4th International Conference on Pervasive Computing and Social Networking (ICPCSN)*. IEEE, 2024, pp. 638–644.

[2] D. Zhang, M. Xu, P. Zhu, C. Guo, Z. Zhong, H. Lu, and Z. Zheng, "The development of a novel terrestrial/aerial robot: autonomous quadrotor tilting hybrid robot," *Robotica*, vol. 42, no. 1, pp. 118–138, 2024.

[3] S. Thorel and B. d'Andréa Novel, "Practical identification and flatness based control of a terrestrial quadrotor," in *2014 IEEE/RSJ International Conference on Intelligent Robots and Systems*. IEEE, 2014, pp. 3221–3226.

[4] N. Pan, J. Jiang, R. Zhang, C. Xu, and F. Gao, "Skywalker: A compact and agile air-ground omnidirectional vehicle," *IEEE Robotics and Automation Letters*, vol. 8, no. 5, pp. 2534–2541, 2023.

[5] Q. Tan, X. Zhang, H. Liu, S. Jiao, M. Zhou, and J. Li, "Multimodal dynamics analysis and control for amphibious fly-drive vehicle," *IEEE/ASME Transactions on Mechatronics*, vol. 26, no. 2, pp. 621–632, 2021.

[6] B. Araki, J. Strang, S. Pohorecky, C. Qiu, T. Naegeli, and D. Rus, "Multi-robot path planning for a swarm of robots that can both fly and drive," in *2017 IEEE International Conference on Robotics and Automation (ICRA)*. IEEE, 2017, pp. 5575–5582.

[7] A. Kalantari and M. Spenko, "Modeling and performance assessment of the hytaq, a hybrid terrestrial/aerial quadrotor," *IEEE Transactions on Robotics*, vol. 30, no. 5, pp. 1278–1285, 2014.

[8] C. Wang, Y. Zhang, C. Li, W. Wang, and Y. Li, "A rotor flywheel robot: land-air amphibious design and control," in *2023 IEEE/RSJ International Conference on Intelligent Robots and Systems (IROS)*. IEEE, 2023, pp. 4341–4346.

[9] Z. Zheng, J. Wang, Y. Wu, Q. Cai, H. Yu, R. Zhang, J. Tu, J. Meng, G. Lu, and F. Gao, "Roller-quadrotor: A novel hybrid terrestrial/aerial quadrotor with unicycle-driven and rotor-assisted turning," in *2023 IEEE/RSJ International Conference on Intelligent Robots and Systems (IROS)*. IEEE, 2023, pp. 6927–6934.

[10] R. Zhang, Y. Wu, L. Zhang, C. Xu, and F. Gao, "Autonomous and adaptive navigation for terrestrial-aerial bimodal vehicles," *IEEE Robotics and Automation Letters*, vol. 7, no. 2, pp. 3008–3015, 2022.

[11] Y. Dong, Y. Zhu, L. Zhang, and Y. Ding, "Tactv: A class of hybrid terrestrial/aerial coaxial tilt-rotor vehicles," *arXiv preprint arXiv:2411.12359*, 2024.

[12] K. Tanaka, D. Zhang, S. Inoue, R. Kasai, H. Yokoyama, K. Shindo, K. Matsuhiro, S. Marumoto, H. Ishii, and A. Takanishi, "A design of a small mobile robot with a hybrid locomotion mechanism of wheels and multi-rotors," in *2017 IEEE International Conference on Mechatronics and Automation (ICMA)*. IEEE, 2017, pp. 1503–1508.

[13] K. Shi, Z. Jiang, L. Ma, L. Qi, and M. Jin, "Mtabot: An efficient morphable terrestrial-aerial robot with two transformable wheels," *IEEE Robotics and Automation Letters*, vol. 9, no. 2, pp. 1875–1882, 2024.

[14] Z. Zheng, Q. Cai, J. Wang, X. Xu, M. Cao, H. Yu, J. Li, J. Meng, and G. Lu, "Capsulebot: A novel hybrid aerial-ground bi-copter robot with two actuated-wheel-rotors," *IEEE Robotics and Automation Letters*, 2024.

[15] K. Li, B. Han, Y. Zhao, and C. Zhu, "Motion planning and simulation of combined land-air amphibious robot," in *IOP Conference Series: Materials Science and Engineering*, vol. 428, no. 1. IOP Publishing, 2018, p. 012057.

[16] W. Ouyang, H. Chi, L. Lu, C. Wang, and Q. Ren, "Motion control of a hybrid quadruped-quadrotor robot," in *Actuators*, vol. 13, no. 6. MDPI, 2024, p. 215.

[17] G. Qin, Y. Xu, W. He, Q. Qi, L. Zheng, H. Hu, Y. Cheng, C. Zuo, D. Zhang, and A. Ji, "Design and development of an air–land amphibious inspection drone for fusion reactor," *Drones*, vol. 8, no. 5, p. 190, 2024.

[18] E. Sihite, A. Kalantari, R. Nemovi, A. Ramezani, and M. Gharib, "Multi-modal mobility morphobot (m4) with appendage repurposing for locomotion plasticity enhancement," *Nature communications*, vol. 14, no. 1, p. 3323, 2023.

[19] M. Bujňák, R. Pirník, K. Rástočnỳ, A. Janota, D. Nemec, P. Kuchár, T. Tichỳ, and Z. Łukasik, "Spherical robots for special purposes: a review on current possibilities," *Sensors*, vol. 22, no. 4, p. 1413, 2022.

[20] R. Chase and A. Pandya, "A review of active mechanical driving principles of spherical robots," *Robotics*, vol. 1, no. 1, pp. 3–23, 2012.

[21] A. H. Javadi A and P. Mojabi, "Introducing glory: A novel strategy for an omnidirectional spherical rolling robot," *J. Dyn. Sys., Meas., Control*, vol. 126, no. 3, pp. 678–683, 2004.

[22] S. Bhattacharya and S. K. Agrawal, "Spherical rolling robot: A design and motion planning studies," *IEEE Transactions on Robotics and Automation*, vol. 16, no. 6, pp. 835–839, 2000.

[23] K. W. Wait, P. J. Jackson, and L. S. Smoot, "Self locomotion of a spherical rolling robot using a novel deformable pneumatic method," in *2010 IEEE International Conference on Robotics and Automation*. IEEE, 2010, pp. 3757–3762.

[24] S. Iyobe, M. Shimizu, and T. Umedachi, "Diverse behaviors of a single-motor-driven soft-bodied robot utilizing the resonant vibration of 2d repetitive slit patterns," *IEEE Robotics and Automation Letters*, vol. 7, no. 2, pp. 992–999, 2021.

[25] A. Kakogawa, S. Jeon, and S. Ma, "Stiffness design of a resonance-based planar snake robot with parallel elastic actuators," *IEEE Robotics and Automation Letters*, vol. 3, no. 2, pp. 1284–1291, 2018.

[26] N. Bucki, J. Tang, and M. W. Mueller, "Design and control of a midair-reconfigurable quadcopter using unactuated hinges," *IEEE Transactions on Robotics*, vol. 39, no. 1, pp. 539–557, 2022.